We are IntechOpen,
the world's leading publisher of
Open Access books
Built by scientists, for scientists

4,800
Open access books available

122,000
International authors and editors

135M
Downloads

Our authors are among the

154
Countries delivered to

TOP 1%
most cited scientists

12.2%
Contributors from top 500 universities

BOOK CITATION INDEX
CLARIVATE ANALYTICS
INDEXED

WEB OF SCIENCE™

Selection of our books indexed in the Book Citation Index
in Web of Science™ Core Collection (BKCI)

Interested in publishing with us?
Contact book.department@intechopen.com

Numbers displayed above are based on latest data collected.
For more information visit www.intechopen.com

Atmospheric Gravity Waves and Effects in the Upper Atmosphere Associated with Tsunamis

Michael P. Hickey
Embry-Riddle Aeronautical University
USA

1. Introduction

Tsunamis propagate at the surface of the deep ocean horizontal phase speeds of approximately 200 m/s, which is about two-thirds of the lower atmospheric sound speed. They have large horizontal wavelengths that are typically of a few hundred kilometers, and they remain coherent over large propagation distances. They also have large horizontal extents (sometimes a few thousand kilometers) parallel to their wave fronts. They can traverse great distances over a span of several hours, so that large areas of the ocean-atmosphere interface are impacted. Typical dominant wave periods associated with tsunamis are a few tens of minutes. In the deep ocean their amplitudes are usually quite small with surface displacements being only a few centimeters, but occasional large events can have amplitudes of a few tens of cm.

The speeds, wavelengths and periods of tsunamis lie within the range of those of atmospheric gravity waves. These are vertically transverse waves with motions of air parcels mainly influenced by gravity and buoyancy. The vertical displacement of the water acts like a moving corrugation at the base of the atmosphere and so very effectively generates atmospheric gravity waves. In general a spectrum of waves will be produced by a tsunami. Most of the power in the spectrum resides in internal gravity waves, with acoustic waves and evanescent waves being less efficiently generated. Internal waves can transport energy and momentum vertically through the atmosphere. Due to the decrease of mean atmospheric density with increasing altitude, the amplitude of these waves increases as they propagate upward in order to conserve wave energy. At sufficiently high altitudes molecular viscosity and thermal conductivity damp the waves, and their amplitudes then decrease with increasing altitude. Because the waves have high phase speeds (commensurate with the tsunami speed), they are deep waves with vertical wavelengths of ~ 100 km. This allows them to reach the middle thermosphere (~ 250 km altitude) before the molecular dissipation becomes severe.

Atmospheric winds also influence the upward propagation of atmospheric gravity waves. Because the winds vary with height the waves may be propagating with the wind at some heights and against the wind at other heights. In the former case the vertical wavelengths are shortened, which increases the velocity shears and thereby increases the viscous damping rate. In the latter case the vertical wavelengths are increased, which decreases the velocity shears and decreases the viscous damping rate.

At these heights the tsunami-driven atmospheric gravity waves have large amplitudes so that their interaction with the ionosphere is likely to produce detectable traveling

ionospheric disturbances (TIDs). These TIDs have been observed in GPS measurements of total electron content and have exhibited a strong correlation with individual tsunami events. Modeling studies have helped the interpretation of such observations. The interaction between the neutral particles and the ions also leads to a further loss of wave energy through ion drag, but viscous effects dominate over ion drag for the typical gravity wave periods associated with tsunamis.

In addition to perturbations of the ionization, the chemistry of the thermosphere is also affected by atmospheric gravity waves. Chemiluminescent airglow emissions associated with neutral and ion chemistry are then affected. These emissions that emanate from a deep region centered at ~ 250 km altitude can be observed from the ground and/or from space. Oblique viewing allows the tsunami-driven disturbances in the thermosphere to be seen from considerable horizontal distances.

Internal atmospheric gravity waves can also transport energy and momentum over considerable vertical distances. The importance of this is due to the considerable decreases of atmospheric density with increasing altitude. In the tenuous upper atmosphere the deposition of small quantities of wave momentum can have a profound effect. Simulations suggest that for large tsunami events the dissipating gravity waves can accelerate the middle thermosphere by ~ 100 m/s within a few hours. These modeling predictions are yet to be confirmed by observations.

In this article observations and modeling of tsunami-driven atmospheric gravity waves are reviewed. Particular emphasis is given to the theory of atmospheric gravity waves, their vertical propagation, and their interaction with the ionosphere and thermospheric chemistry. The ability to measure a disturbance at a large distance from the tsunami offers a means of early detection to augment other early warning measurements. The utility of modeling and simulation in the interpretation of such tsunami-driven disturbances in the thermosphere is demonstrated.

2. Atmospheric acoustic-gravity waves

Around the dawn of the twentieth century with the advent of radio wave communications came the subsequent discovery of the ionosphere. New research was initiated related to ionospheric physics and chemistry and many new discoveries followed. One of these was the existence of traveling ionospheric disturbances (TIDs), which were ionospheric irregularities propagating rapidly in the horizontal direction with speeds of many tens to hundreds of m/s, and often with large horizontal wavelengths of 100s of km (Munro, 1948). Martyn (1950) was the first to explain the TIDs in terms of internal atmospheric gravity waves, and Hines (1960) finally produced a correct and unambiguous description of the phenomenon in terms of these waves.

Atmospheric gravity waves are fluctuations of the neutral atmosphere, usually triggered by events that cause a lifting of localized regions of the atmosphere. In the lower atmosphere sources of gravity waves include severe weather systems (Georges, 1968), and winds blowing over mountains (Scorer, 1949). A more complete discussion of these and other sources is given by Fritts and Alexander (2003). Gravity waves are the low frequency component of the more general class of acoustic-gravity waves. The acoustic waves, of higher frequencies than gravity waves, are primarily driven by events that produce a rapid compression of a region of the atmosphere. We remark that compressional effects are also important for high frequency gravity waves. At very high altitudes the oscillatory motion of

air particles associated with gravity waves causes the ionospheric ions (and electrons) to oscillate due to neutral-ion collisions. The ion-electron motions are constrained by the geomagnetic field, chemistry, and electric fields.

The initial theory of acoustic-gravity waves of Hines (1960) was based on an idealized atmosphere (windless, isothermal, adiabatic wave motions). This important study showed that internal atmospheric gravity wave amplitudes will grow exponentially with increasing height as the waves propagate upward in order to conserve wave energy. If mean pressure and density decrease exponentially as $e^{-z/H}$ (where H is the atmospheric scale height), then wave amplitudes grow as $e^{z/2H}$. Due to the fact that the mean atmospheric density decreases by a factor of $\sim 10^6$ between sea level and the lower thermosphere (near 100 km altitude), wave amplitudes will increase by a factor of $\sim 10^3$ during the upward propagation of the waves over this region. A dispersion relation was derived relating the vertical wavelength ($\lambda_z = 2\pi/m$) to the horizontal wavelength ($\lambda_x = 2\pi/k$) and wave period ($T = 2\pi/\omega$)

$$m^2 = k^2\left(\frac{N^2}{\omega^2} - 1\right) - \frac{\left(\omega_a^2 - \omega^2\right)}{C^2} \tag{1}$$

Here, ω is the wave frequency, m is the vertical wavenumber, and k is the horizontal wavenumber. Also, C ($\sqrt{\gamma g H}$) is the sound speed, N is the Brunt-Väisälä frequency (for an isothermal atmosphere $N^2 = (\gamma - 1)g^2/C^2$), and ω_a ($= \gamma g/2C$) is the acoustic cut-off frequency. Also, γ is the ratio of specific heats and g is the gravitational acceleration. Inspection of Equation (1) reveals that internal waves (those with real m) exist for either $\omega < N$ (gravity waves) or for $\omega > \omega_a$ (acoustic waves). For intermediate wave frequencies $N < \omega < \omega_a$ only evanescent waves exist. Internal waves ($m^2 > 0$) can transport energy and momentum vertically through the fluid in which they propagate, but evanescent waves ($m^2 < 0$), of which surface waves are a subset, cannot. Typically, gravity waves have periods ranging from ~ 10 min to a few hours, and horizontal wavelengths ranging from a few tens of km to several hundreds of km (occasionally even larger). They propagate with phase speeds of tens to hundreds of m/s, and are subsonic. Because of this, the slower gravity waves tend to have lower atmospheric sources (where the sound speed is lower), while fast gravity waves have high altitude sources where the sound speed is high. Gravity waves are vertically-transverse waves primarily influenced by the competing effects of gravity and buoyancy.

To help better understand the propagation of gravity waves we next examine the atmospheric mean state. Figure 1a shows altitude profiles of the mean temperature (T) obtained from the MSIS-90 model (Hedin, 1991), and the derived Brunt-Väisälä period (τ_B) and the sound speed C. The conditions are appropriate for the equator at times of low solar and geomagnetic activity (see Hickey et al., 2009). The temperature increases rapidly in the lower thermosphere, and asymptotes to a value of ~ 753 K in the upper thermosphere. In the thermosphere τ_B increases rapidly with increasing height and asymptotes to a value of ~ 12 min at high altitudes. Hence gravity waves having periods exceeding ~ 12 min will be internal at all heights ($\omega < N$ everywhere). The altitude variation of τ_B suggests that waves with periods satisfying 4 min ≤ T ≤ 12 min will be evanescent over some altitude range and

so would have diminished amplitudes at high altitudes. Hence, gravity waves with periods exceeding ~ 12 min should dominate the F-region (near 300 km altitude) response to an upward propagating gravity wave disturbance. The sound speed profile suggests that gravity waves of lower atmosphere origin will have phase speeds of less than about 300 m/s.

The corresponding mean winds used in our model, obtained with the HWM93 model (Hedin et al., 1996), are shown in Figure 1b. The meridional winds remain relatively small at most altitudes, with a maximum value of ~ 30 m/s (northward) near 250 km altitude. The zonal winds are much larger in the thermosphere, and approach 70 m/s (eastward) at high altitudes. Because the tsunami-generated gravity waves are fast (~ 200 m/s), we expect them to be relatively unaffected by the meridional winds. On the other hand, the zonal winds are expected to influence the gravity waves.

3. Tsunami-related upper atmosphere observations

Hines (1972) first postulated that tsunamis may be capable of producing atmospheric gravity waves that could subsequently propagate to high altitudes. Later, Peltier and Hines (1976) demonstrated the plausibility of this idea using a simple model of a gravity wave disturbance. The subject of tsunami-generated gravity waves remained relatively unexplored until the observations of Artru et al. (2005). They used Global Positioning System (GPS) measurements of total electron content (TEC) following the earthquake of Peru on June 23, 2001, and showed that the observed ionospheric disturbance had similar characteristics to the expected tsunami-generated gravity wave. In particular, they derived a horizontal propagation velocity of ~ 150 m/s in a direction consistent with the source location. Ionospheric observations showing evidence of gravity waves following the December 26 2004 Sumatra tsunami were reported by Liu et al. (2006a, b) and by DasGupta et al. (2006). Lee et al. (2008) observed large ionospheric variations with accompanying spread F over Arecibo on the evening of December 26 2004. They postulated that tsunamigenic gravity waves associated with the Sumatra event were responsible for the observations.

4. Modeling gravity wave propagation

4.1 Previous modeling

Artru et al. (2005) used the basic theory developed by Hines (1960) to model gravity wave propagation and to provide a match to their observations. Ionospheric perturbations were not specifically modeled. However, by deriving the group velocities for the disturbances they were able to obtain good agreement between modeled and observed propagation times for the disturbances.

Occhipinti et al. (2006) performed time-dependent modeling of the December 26th 2004 Sumatra tsunamigenic gravity waves assuming that the atmospheric wave motions were inviscid and adiabatic. The ocean sea surface displacement was defined using a model of Hébert et al. (2007). A nonlinear ionospheric perturbation model was also included in order to be able to simulate the observed TEC observations. They found that the ionospheric response depended sensitively on the magnetic latitude (as described in the earlier work of Hooke, 1968). The relative TEC perturbation amplitudes were about 10%, which was noted to be in agreement with the observations of Liu et al. (2006b). Their results were also found to be largely insensitive to the effects of ion chemistry and diffusion. Occhipinti et al. (2008) continued from their previous work with a strong focus on the latitudinal variation of the
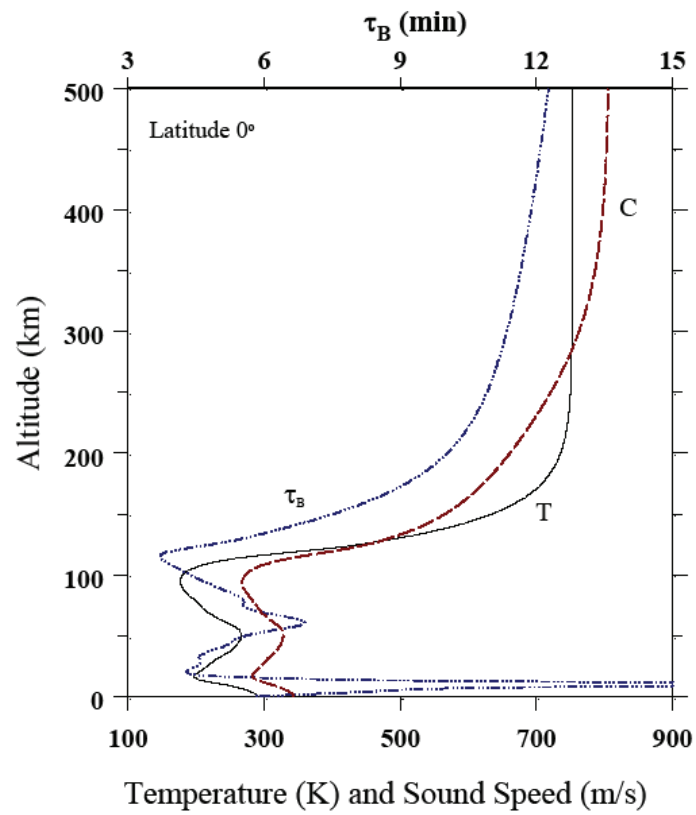
Fig. 1a. Mean temperature (*T*, in K), sound speed (*C*, in m/s) and Brunt-Väisälä period (τ_B, in min). After Hickey et al. (2009)
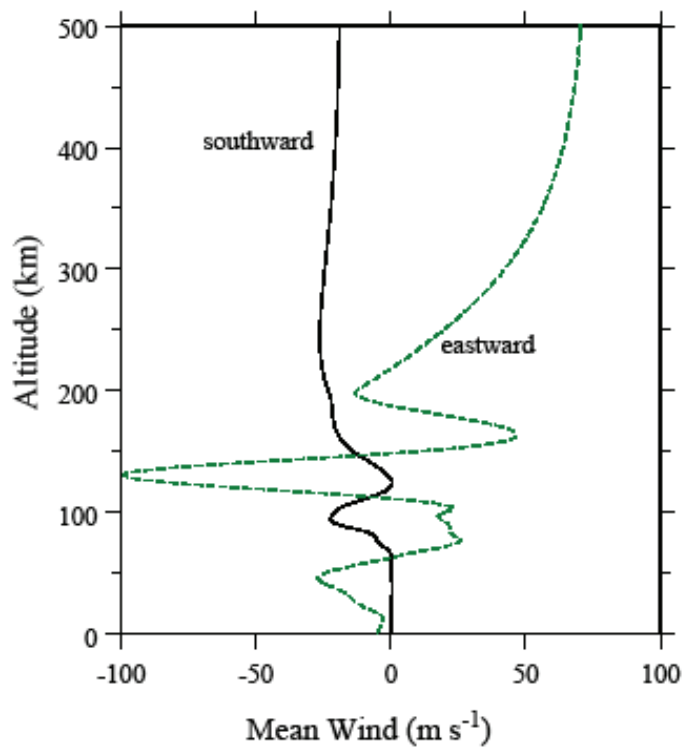

Fig. 1b. Mean southward and eastward winds (m/s). After Hickey et al. (2009)

ionospheric response to a tsunamigenic gravity wave. A clear anisotropic response was noted in their derived TEC perturbations. Note that their model used the Boussinesq approximation which applies to low frequency gravity waves for which the perturbations can be assumed to be incompressible; hence the model is essentially the same as that of Occhipinti et al. (2006).

4.2 Full-wave model description

The full-wave model, described below, has been previously used to model acoustic wave (Hickey et al., 2001; Schubert et al., 2005; Walterscheid and Hickey, 2005) and gravity wave (Hickey et al., 1997; Walterscheid and Hickey, 2001) propagation in Earth's atmosphere. A Cartesian coordinate system is used with *x*, *y* and *z* directed southward, eastward, and upward, respectively. The unperturbed mean state atmosphere is assumed to vary only in the vertical direction and is specified using the MSIS model (Hedin, 1991). For the simulations discussed later the lower boundary of the model is at the ground (*z*=0) and the upper boundary is at *z*=600 km.

The model solves the Navier-Stokes equations for steady, linear waves propagating in an atmosphere that is horizontally homogeneous and stratified vertically. The mean, undisturbed state is non-isothermal, and mean winds are a function of height. The model includes the eddy and molecular diffusion of heat and momentum, ion drag, Rayleigh friction and Newtonian cooling, and the Coriolis force. The momentum equation is

$$\rho \frac{D\bar{v}}{Dt} + \underline{\nabla} p - \rho \bar{g} + 2\rho \bar{\Omega}_E \times \bar{v} + \underline{\nabla} \cdot \underline{\underline{\sigma}} - \underline{\nabla} \cdot \left(\rho \eta_e \underline{\nabla} \bar{v} \right) - \rho \nu_{ni} \left(\bar{v}_i - \bar{v} \right) + \rho K_R \bar{v} = 0 \tag{2}$$

In this equation ρ is mass density, $\bar{v}$ is velocity, p is pressure, $\bar{g}$ is the gravitational acceleration, $\bar{\Omega}_E$ is the Earth's angular frequency, $\underline{\underline{\sigma}}$ is the viscous stress tensor, η_e is the eddy diffusivity, ν_{ni} is the neutral-ion collision frequency, $\bar{v}_i$ is the ion velocity, and K_R is the Rayleigh friction coefficient. Also, $D/Dt = \partial/\partial t + \bar{v} \cdot \underline{\nabla}$ is the substantial derivative, where t is time. The viscous stress tensor is defined as

$$\sigma_{ij} = -\mu_m \left(\frac{\partial v_i}{\partial x_j} + \frac{\partial v_j}{\partial x_i} - \frac{2}{3} \delta_{ij} \underline{\nabla} \bar{v} \right) \tag{3}$$

where μ_m is the dynamic viscosity and δ_{ij} is the Kroneka delta. The energy equation is

$$\rho c_v \frac{DT}{Dt} + p \underline{\nabla} \cdot \bar{v} + \underline{\underline{\sigma}} : \underline{\nabla} \bar{v} - \underline{\nabla} \cdot \left(\lambda_m \underline{\nabla} T \right) - \frac{c_p T}{\theta} \underline{\nabla} \cdot \left(\rho \kappa_e \underline{\nabla} \theta \right) - \rho \nu_{ni} \left(\bar{v}_i - \bar{v} \right)^2 + \rho c_v K_N T = 0 \tag{4}$$

Here T is temperature, λ_m is the coefficient of thermal conductivity, c_p and c_v are the specific heats at constant pressure and constant volume, respectively, κ_e is the eddy diffusivity of heat, and K_N is the Newtonian cooling coefficient. In these studies we set K_N equal to K_R. At the upper boundary they serve as a sponge layer and are set equal to the wave frequency; at lower altitudes they decrease exponentially away from the upper boundary with a characteristic scale height of 50 km ($K_N = \omega \exp\left[(z - 600km)/50km\right]$. The

potential temperature is defined as $\theta = T\left(p_{00}/p\right)^{R/c_p}$, where R is the gas constant and p_{00} is a reference pressure (taken to be the sea-level value).

The continuity equation is

$$\frac{D\rho}{Dt} + \rho\underline{\nabla}\cdot\bar{v} = 0 \tag{5}$$

The linearized equation of state for an ideal gas ($p'/\bar{p} = \rho'/\bar{\rho} + T'/\bar{T}$) completes the set. Here primes denote perturbation values and the over-bar signifies the mean state.

The solution procedure involves first linearizing Eqs. (2) through (5), and then eliminating density perturbations (ρ') using the linearized ideal gas equation of state. Next, plane wave solutions of the form $\exp i\left(\omega t - kx - ly\right)$ are assumed, where ω is the wave frequency, t is time, and k and l are the wavenumbers in the x and y directions, respectively. This allows the terms involving time and horizontal derivatives to be replaced by algebraic terms. The remaining system of equations is essentially a set of coupled second order differential equations in the vertical coordinate, z. A complete listing of these equations is provided in the appendix of Schubert et al. (2003) and by Hickey et al. (2004). These equations are then written in their finite-difference form and solved using a method described by Bruce et al. (1953), as modified by Lindzen and Kuo (1969). At the upper boundary (z=600 km) a radiation condition is assumed with solutions provided using a dispersion equation described by Hickey and Cole [1987]. The lower boundary (ground) condition allows the vertical velocity to be specified. The equations are solved on a high resolution grid with the vertical spacing chosen to be typically several meters. The input required for the model is the altitude profile of the mean state (temperature, density, molecular weight, and horizontal winds), the wave amplitude, period, horizontal wavelength and direction of propagation. The model produces altitude profiles of amplitude and phase for the perturbations (three velocity components, temperature and pressure). From these other quantities of interest can be calculated, such as momentum, sensible heat and energy fluxes and their divergence.

4.3 Spectral full-wave model

The approach of Peltier and Hines (1976) is used to model the propagation of a tsunami-generated gravity wave disturbance. The following description is also provided in Hickey et al. (2009). The initial (t=0) displacement Z at the sea surface (z=0) is prescribed by

$$Z(x, z = 0, t = 0) = A\left\{Ai(-x+1)\frac{x}{2}\exp[-(x-2)/2]\right\} \tag{6}$$

where Ai is the Airy function, and x is the horizontal position in units of 100 km. The amplitude of the forcing is A (in meters). The Fourier transform of (6) provides the wavenumber (k) spectrum of the forcing

$$\hat{Z}(k, 0, 0) = \frac{1}{2\pi}\int_{-\infty}^{\infty} Z(x, 0, 0)e^{ikx}dx \tag{7}$$

Our simulations are based on long wavelength water waves propagating on the ocean surface. They are nondispersive and propagate with the shallow water phase speed

$c = \sqrt{gh}$, where g is the gravitational acceleration and h is the ocean depth (Lighthill, 1978). The tsunami is taken to propagate in the negative x-direction (but this is later altered to accommodate propagation in any arbitrary direction) in an ocean of depth 4 km. Hence $c = -200$ m/s, whence $\omega = -200k$. The vertical velocity spectrum is then given by

$$\hat{W}(k,0,0) = i\omega\hat{Z}(k,0,0) = -i200k\hat{Z}(k,0,0) \tag{8}$$

We use a discrete Fourier transform to evaluate the spectrum of the surface displacement $\hat{Z}$ and the vertical velocity spectrum $\hat{W}$. Figures 1a and 1b show the surface displacement (Z) and the vertical velocity spectrum ($\hat{W}$).

Occhipinti et al. (2006) reported sea surface displacements measured by Jason-1 and Topex-Poseidon that were characterized by a dominant horizontal scale size of 400 km and an amplitude of ~ 0.5 m. Wilson (2005) reported similar values (~ 500 km and 0.3 to 0.6 m, respectively). In Hickey et al. (2009) and here we adopt the former set of values. The amplitude of the surface displacement shown in Figure (2a) initially increases rapidly and diminishes after several cycles. The vertical velocity spectrum shown in Figure 2(b) is characterized by maxima at ± 400 km, corresponding to a dominant period of 33 min. This is in general agreement with the analysis of tide gauge measurements in and near the Indian Ocean that revealed periods ranging from 10 to 60 min and a dominant period of 40 min for the Sumatra tsunami event (Abe, 2006).

The full-wave model output is obtained for each discrete wave (ω-k) in the spectrum, with the vertical velocity at the lower boundary (z=0) specified to be unity. If we denote this output by $\psi'_j(\omega,k,z)$ (here the subscript j denotes each of velocity, temperature or pressure), then the response to the forcing is given by

$$\Psi'_j(x+vt,z) = \frac{1}{2\pi}\int_{-\infty}^{\infty}\hat{W}(k,0,0)\psi'_j(\omega,k,z)e^{-ik(x+vt)}dk \tag{9}$$

Note that the product $\hat{W}(k,0,0)\psi'_j(\omega,k,z)\Delta k$ represents the response of a single wavenumber-dependent perturbation to the spectral forcing, where Δk is the bandwidth. Because the Brunt-Väisälä period (τ_B) exceeds ~4 min everywhere (see Figure 1), waves of period ~3 to ~4 min will experience evanescence over much of the lower and middle atmosphere and so will be unable to propagate to the thermosphere. Waves of acoustic periods will not be efficiently generated by the tsunami, and moreover they will be evanescent because their phase speeds are less than the sound speed throughout the atmosphere. Hence we truncate the spectrum and include waves having periods of 3 min (wavelength 36 km) and longer. Equation (9) was solved using 800 waves (400 positive k and 400 negative k) for values of x ranging from -1000 km to +14400 km (and Δk = 4.36 x 10^{-7} m^{-1}).

4.4 Ion-electron perturbation model

The modeled electron-ion response to a linear gravity wave includes the effects of dynamics and chemistry. We use a solution procedure similar to that previously used to model the response of minor species and related airglow emissions in the mesospause region to gravity wave forcing (Walterscheid et al., 1987; Hickey, 1988).
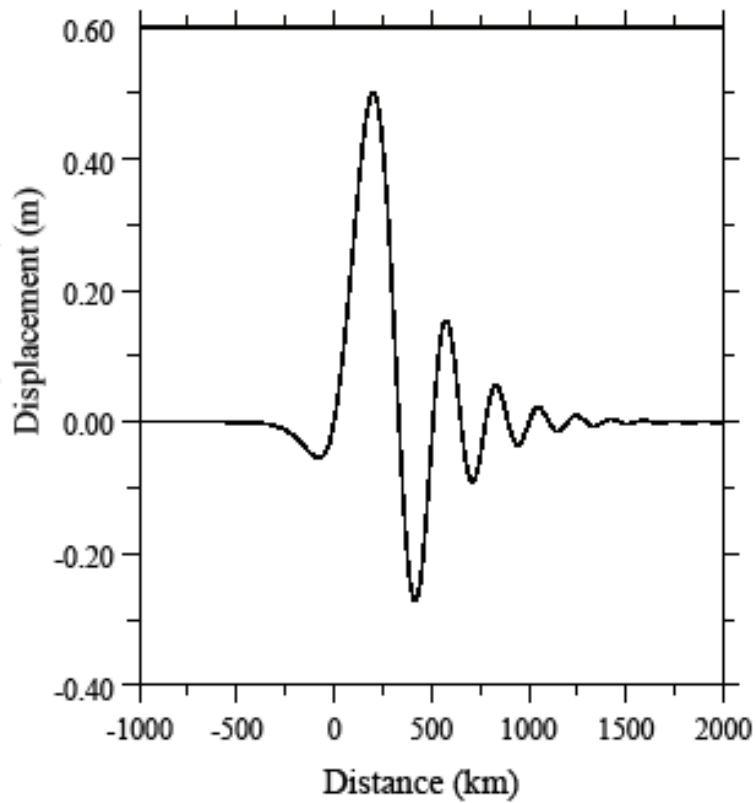
Fig. 2a. Surface displacement (after Hickey et al., 2009)
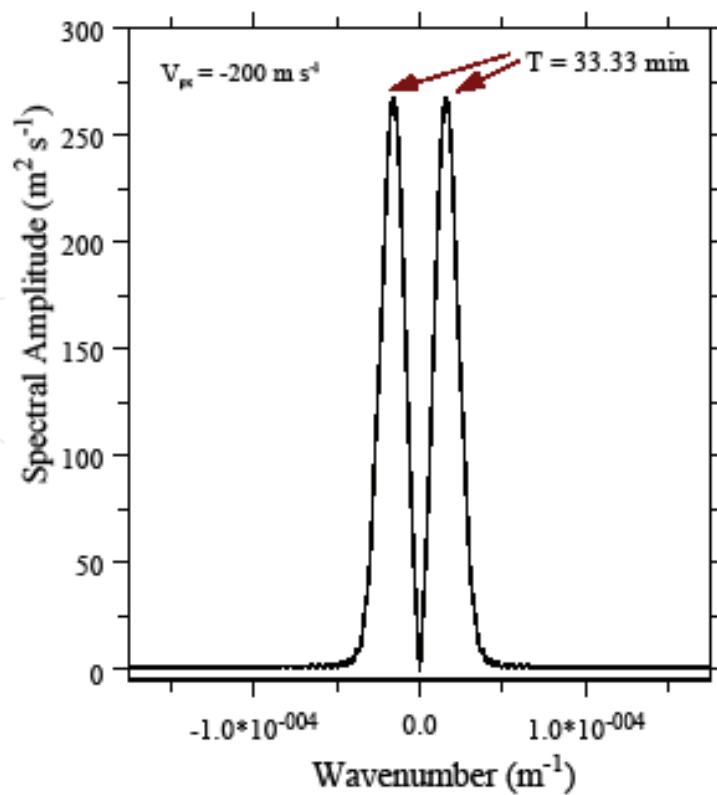

Fig. 2b. Vertical velocity spectrum at model lower boundary (after Hickey et al., 2009)

The linearized perturbation ion continuity equations for each of the ion species O^+, O_2^+, N_2^+ and NO^+ (n_j) are

$$i\omega n'_j + w'_j \frac{d\overline{n}_j}{dz} + \overline{n}_j \underline{\nabla} \cdot v'_j = P'_j - \overline{n}_j L'_j - n'_j \overline{L}_j \tag{10}$$

Here, P and L are the chemical production and loss rates, respectively. They are calculated based on the set of chemical equations of Schunk and Sojka (1996), given in Appendix 1 (as in Hickey et al., 2010a). The electron density profile is based on a Chapman layer, with a maximum value of 10^{12} m^{-3} at 300 km altitude.

For the ion momentum equation we follow the approach of McLeod (1965) and neglect polarization electric fields, gravity and diffusion:

$$\overline{v}_i = \left(\omega_i^2 + \nu_{in}^2\right)^{-1} \left\{ \nu_{in} \omega_i \overline{v} x \hat{B} + \omega_i^2 (\overline{v} \cdot \hat{B}) \hat{B} + \nu_{in}^2 \overline{v} \right\} \tag{11}$$

Here $\omega_i = q_i B / M_i$ is the ion gyrofrequency and $\nu_{in} = 2.6 x 10^{-15}(n_n + n_i) A^{-1/2}$ (*Kelley*, 1989) is the ion-neutral collision frequency, and where q_i and M_i are the charge and atomic or molecular weight, respectively of the ion, B is the magnetic field strength in Gauss (Wb/m^2), and n_n and n_i are the neutral and ion number density, respectively. Given the gravity wave perturbation velocity $\underline{v}'$, Eq. (11) is used to determine $\underline{v}'_j$ for each of the four ions. These ion velocities are then substituted in Eq. (10), and the system of four equations is inverted to yield the perturbation ion number densities. Other details of the calculations are provided in Hickey et al. (2009), and are not repeated here.

5. Results

5.1 Electron fluctuations

We begin by showing the results for the dominant wave in the spectrum. This wave has a period of ~ 33 min and a horizontal wavelength of 400 km. It is forced at the lower boundary of the full-wave model with a vertical velocity amplitude of 1.17×10^{-4} m s^{-1}. Mean winds, ion drag and Coriolis force are not included in this simulation, and so the propagation occurs isotropically in the horizontal direction.

The vertical velocity and temperature perturbation amplitudes are shown as a function of height in Figure 3a for two cases. In the first case the nominal viscosity and thermal conduction parameters are used, while in the second case these parameters are reduced by several orders of magnitude in order to mimic negligible dissipation (the adiabatic case). In the adiabatic case wave amplitudes increase by a factor of 10^6 over the altitude range shown in order to conserve wave energy. In the case of nominal dissipation the waves eventually dissipate and achieve a maximum amplitude near 200 km altitude. The phase of the vertical velocity fluctuations is shown as a function of height in Figure 3b. This figure demonstrates that at high altitudes the dissipation causes an increase in the vertical wavelength of the waves. Up to about 250 km altitude the vertical wavelength is ~ 100 km in both cases, but at high altitudes the vertical wavelength becomes very large in the non-adiabatic case.

The resulting O^+ velocity components for this wave are shown in Figure 4a. In this case we have included ion drag and the Coriolis force, and simulations are performed for the wave propagating either northward or eastward at the equator. The largest ion response occurs
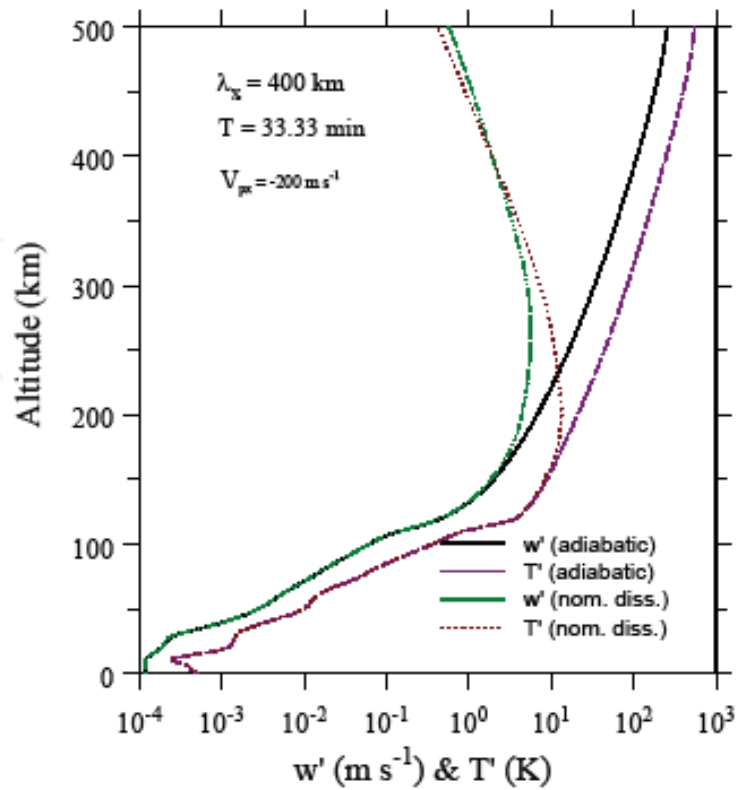
Fig. 3a. Vertical velocity and temperature perturbation amplitudes for adiabatic and non-adiabatic waves of 400 km horizontal wavelength and 33 min period (after Hickey et al., 2009)
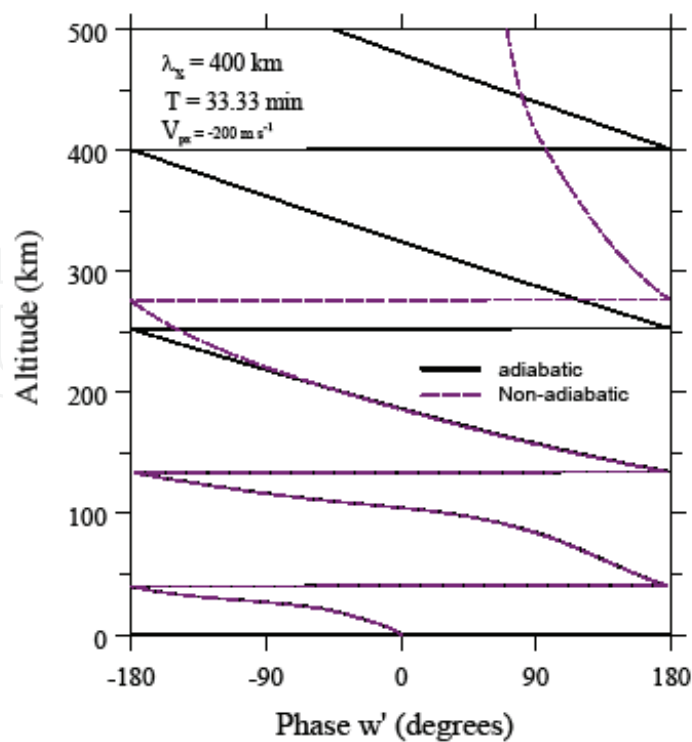

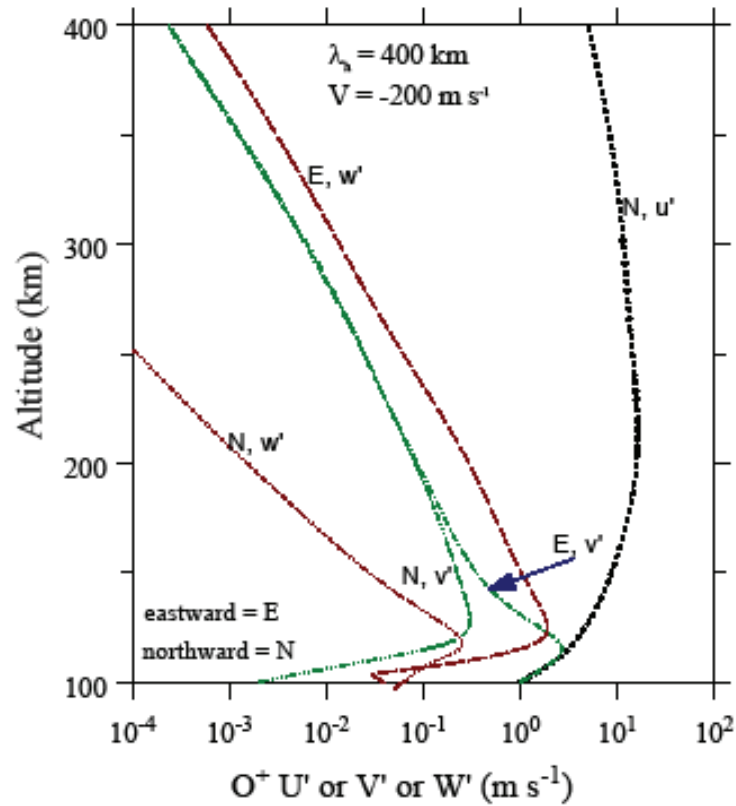Fig. 3b. As in Figure 2a except for the phases (after Hickey et al., 2009)

Fig. 4a. Ion velocity components for O⁺ for northward and eastward propagating waves at the equator (after Hickey et al., 2010a)
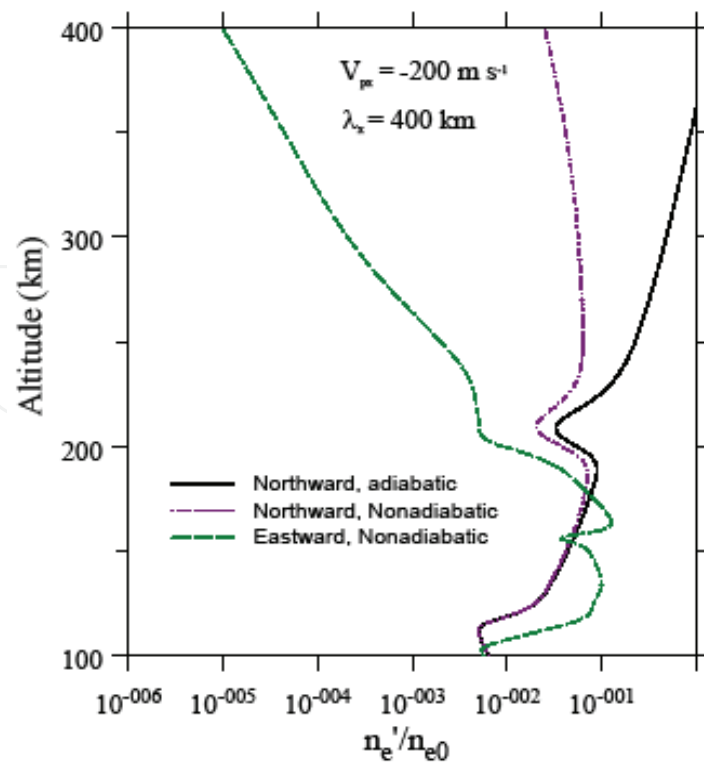

Fig. 4b. (after Hickey et al., 2009)

for northward wave propagation and for the meridional perturbation velocity (of ~ 15 m/s at 200 km altitude). By comparison, the ion velocity response is small for an eastward propagating wave, and is largest for the vertical ion velocity (~ 0.2 m/s at 200 km altitude). The associated electron density response is shown in Figure 4b. For realistic dissipation (nonadiabatic case) the largest response (of ~ 7% of the mean at 300 km altitude) occurs for the northward propagating wave. With small dissipation and for the northward propagating wave the electron density response is about an order of magnitude larger than this.
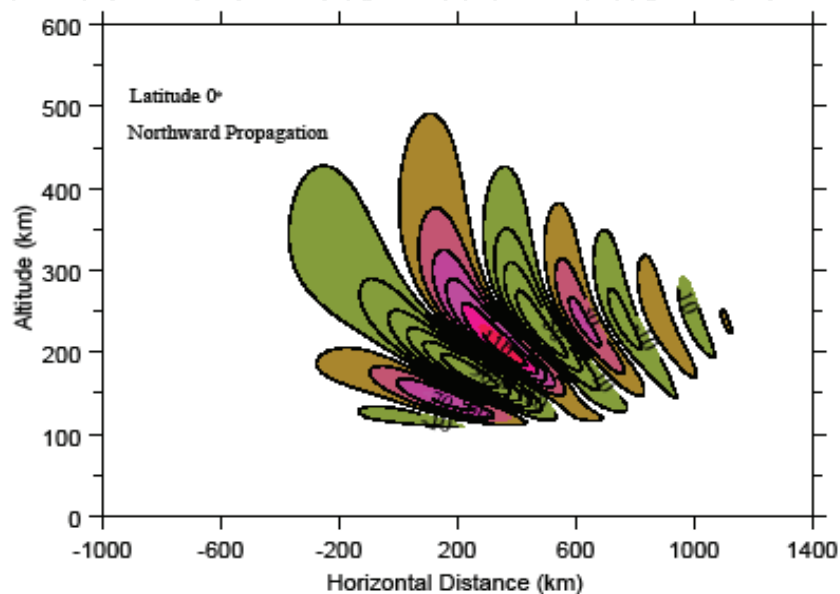
Fig. 5a. Temperature fluctuation (in K) for a northward propagating gravity wave disturbance (after Hickey et al., 2010a)
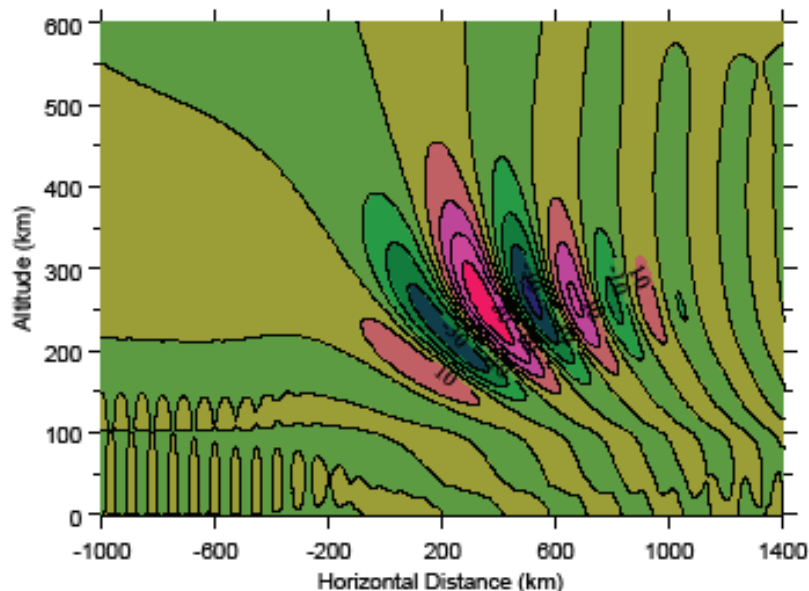
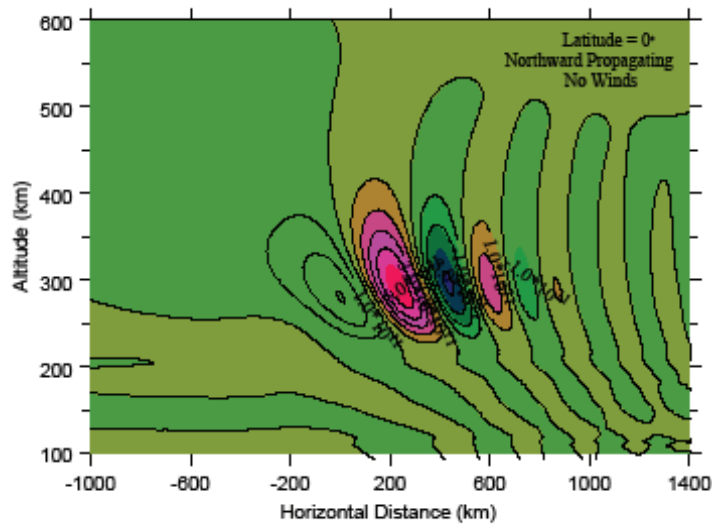Fig. 5b. Vertical velocity fluctuation (in m/s) for a northward propagating gravity wave disturbance

Fig. 6a. Electron density perturbations for northward propagation including dissipation and without mean winds (after Hickey et al., 2009)
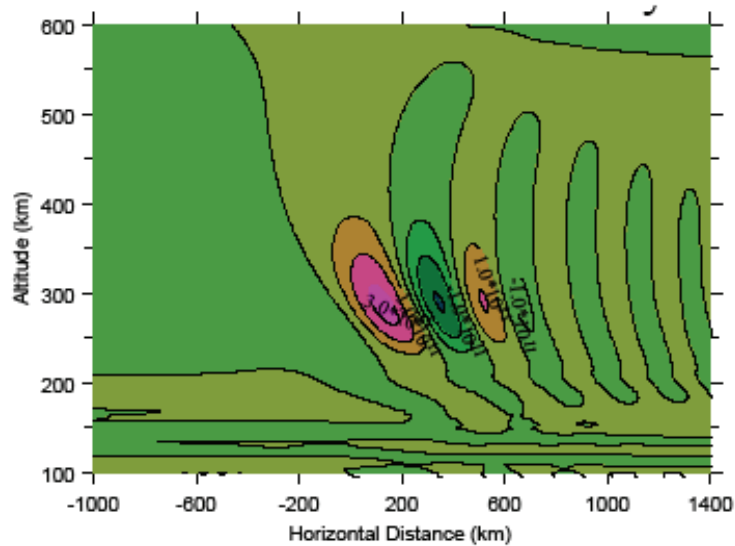

Fig. 6b. As in Figure 6a, except with the inclusion of mean winds (after Hickey et al., 2009)

The results of the spectral full-wave model are now discussed. Figure 5a shows the temperature fluctuation as a function of height and horizontal position for a northward propagating gravity wave disturbance with realistic dissipation included. The maximum perturbation of ~ 130 K (which is about 20% of the mean, undisturbed temperature) occurs over the 200 to 250 km altitude region. At greater heights the phase fronts become more vertical as a consequence of the increasing dissipation due to viscosity and thermal conduction (Hines, 1968). Figure 5b shows the corresponding vertical velocity fluctuation. The maximum of ~ 30 m/s occurs near 300 km altitude. About two to three dominant cycles are evident in these results.

Next we examine the effects of mean winds on the electron density response for a northward propagating gravity wave disturbance with realistic dissipation. Figure 6a shows the electron density response as a function of height and horizontal position without mean

winds included. The maximum perturbations occur at the F2 peak near 300 km altitude and are localized to a horizontal region of ~ 800 km extent (which is twice the dominant horizontal wavelength). The maximum perturbation is ~ 60% of the mean at x ~ 200 km. With the further inclusion of mean winds (Figure 6b) the maximum perturbation is ~ 30% of the mean, while the horizontal extent of the disturbance has been reduced.

In order to simulate GPS observations, we have performed vertical integrations of the electron density perturbations to obtain the total electron content (TEC) perturbations. The integration of the mean, undisturbed electron density profile gives a TEC value of 17 TECU (where 1 TECU = 10^{16} electrons/m^2). For northward propagation (Figure 7a), TEC fluctuations are largest for the quasi-adiabatic, windless case. The inclusion of dissipation reduces the TEC fluctuation amplitude and also alters the phase of the disturbance. The further inclusion of mean winds alters the phase again, and causes a further reduction in the amplitude of the perturbations. In this latter (and more realistic) case the maximum TEC perturbations are about 3 TECU, which corresponds to an approximate 20% perturbation about the mean.

The results for an eastward propagating wave disturbance are shown in Figure 7b. Immediately evident is the significantly smaller response than for the northward propagating disturbance. As before, the smallest response occurs when dissipation and mean winds are included, and the maximum amplitude is ~ 0.01 TECU. It should be noted that these results apply to the equator. At mid-latitudes the ionospheric response to a zonally propagating gravity wave disturbance will be much larger, and can be comparable to that obtained for a meridionally propagating gravity wave disturbance (Occhipinti et al., 2008). This is because the vertical velocity fluctuation has a component parallel to the geomagnetic field at mid-latitudes, which can thus impart ion motion in that direction.

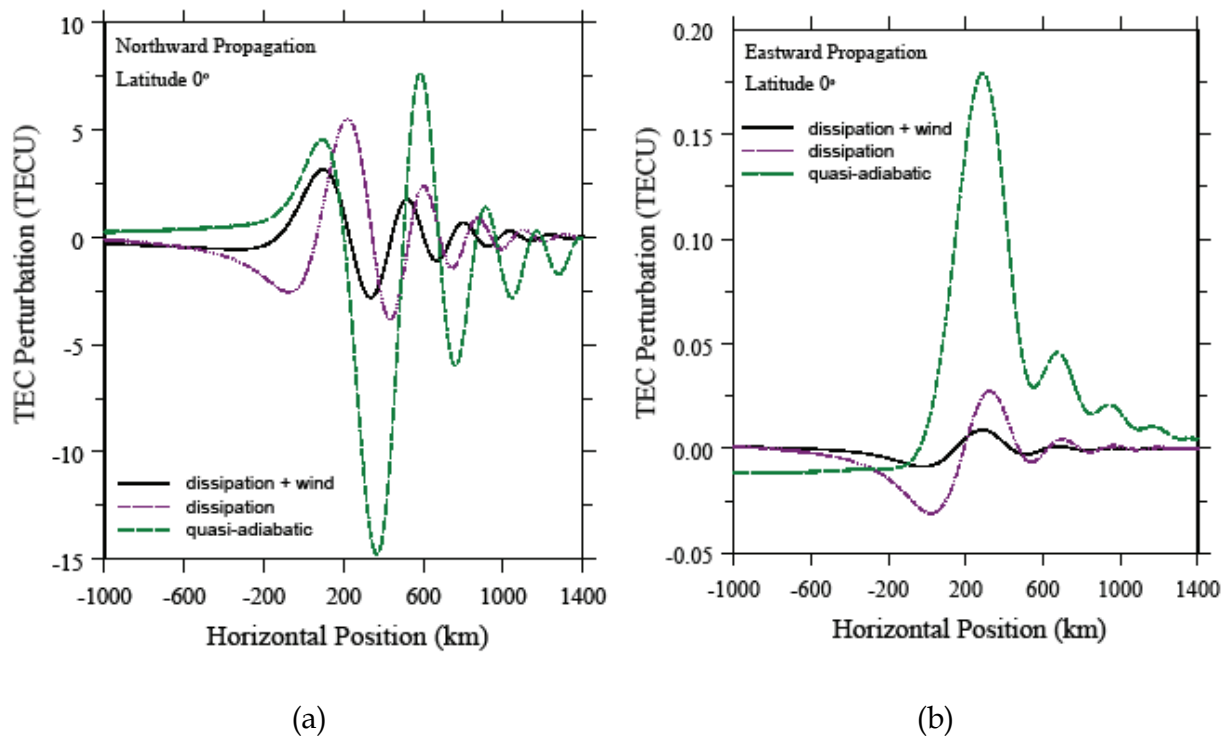(a)   (b)

Fig. 7. (a) TEC fluctuations for northward propagation (after Hickey et al., 2009). (b) TEC fluctuations for eastward propagation (after Hickey et al., 2009).

5.2 Airglow fluctuations

Atmospheric gravity waves propagating in the thermosphere are known to produce airglow variations associated with the wave-perturbed chemistry. Gravity wave motions have been detected in the 6300 A (red-line) nightglow (e.g., Sobral et al., 1978; Mendillo et al., 1997; Kubota et al., 2001), and also in the far-ultraviolet (FUV) O 1356 A emission (Paxton et al., 2003; DeMajistre et al., 2007). The chemistry associated with these emissions is included in Table 1 in Appendix 1. The mean undisturbed electron density profile is shown in Figure 8. Also shown are the altitude profiles of the mean undisturbed volume emission rates (VER) for these two emissions. The O 1356 Å VER peaks near 300 km altitude with a value of ~ 7.2 x 10^5 photons/s/m^3, and the OI 6300 Å VER peaks near 254 km altitude with a value of ~ 8.6 x 10^7 photons/s/m^3. The former profile is broader in its altitude extent than the latter.

The resulting OI 6300 Å VER perturbations for northward propagation at the equator, with nominal dissipation and in the absence of mean winds are shown as a function of height and horizontal position in Figure 9. For this particular gravity wave disturbance the perturbations maximize in the vicinity of the altitude where the mean undisturbed OI 6300 Å VER (shown in Figure 8) maximizes. The maximum value of the perturbation VER is ~6 x 10^7 photons/s/m^3, which is about 70% of the mean undisturbed value. Two complete cycles of the disturbance are evident in the VER fluctuations. Note that although we do not show the O 1356 Å VER perturbations, they resemble those for the OI 6300 Å except the maxima occur closer to 300 km altitude, in the vicinity of the peak undisturbed O 1356 Å profile (see Hickey et al., 2010a).
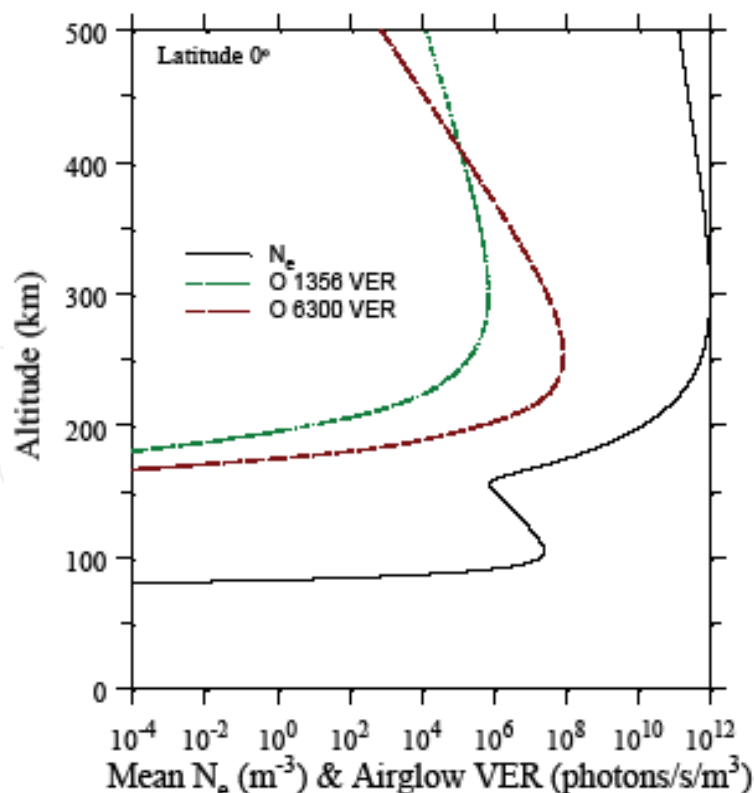

Fig. 8. Mean electron density (m^{-3}), mean OI 6300 Å VER (photons/s/m^3), and mean O 1356 Å VER (photons/s/m^3) (after Hickey et al., 2010a)
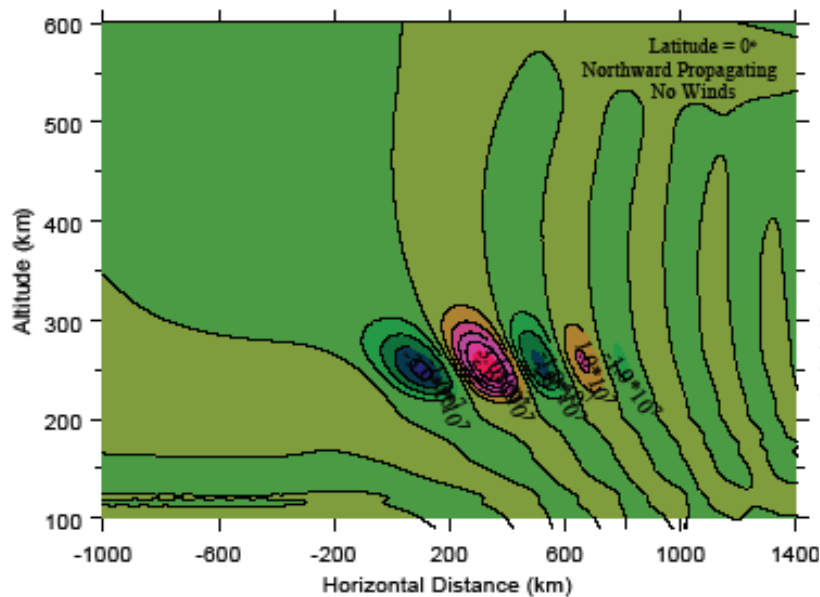
Fig. 9. OI 6300 Å VER fluctuations as a function of altitude and horizontal position (after Hickey et al., 2010a)

The brightness fluctuations are now obtained by integration over altitude of the VER fluctuations. We have done so for both the OI 6300 Å and the O 1356 Å emissions. We have also performed two integrations, one vertically, and the other along an oblique slant path inclined at an angle of ~29º from the horizontal. In each case we have then normalized the brightness fluctuations to the mean undisturbed brightness to obtain the relative brightness fluctuations (see Figure 10). The maximum relative brightness fluctuations for the OI 6300 Å emission (Figure 10a) are ~50% for overhead viewing and 25% for oblique viewing. The maximum occurs almost 400 km earlier for the oblique viewing, which equates to a time difference of ~ 30 minutes. Hence, for oblique viewing the disturbance could be observed approximately 30 minutes earlier compared to overhead viewing.

Similar results are seen for the O 1356 Å emission (Figure 10b). The relative brightness fluctuation is smaller for oblique viewing (~18% versus 43%), but appears ~ 400 km (corresponding to ~30 minutes) earlier than for overhead viewing. Also shown in this figure are the relative TEC fluctuations for overhead and oblique viewing. They strongly resemble the O 1356 Å fluctuations in terms of amplitude and phase. For overhead viewing both waveforms look strikingly similar to the original lower boundary/tsunami disturbance shown in Figure 2a. The maximum relative TEC fluctuations are ~ 33% and 8% for overhead and oblique viewing, respectively.

5.3 Momentum transport

Atmospheric gravity waves transport momentum and sensible heat. The respective fluxes per unit volume of these quantities are given by $F_m = \bar{\rho}\langle u'w' \rangle$ and $F_{sh} = \bar{\rho}c_p\langle w'T' \rangle$, where all symbols are as previously defined, and where the brackets denote an average over a complete horizontal wavelength of the wave disturbance. Here we will focus primarily on the momentum flux and its possible impact on the thermosphere. The impact of the sensible heat flux will be briefly summarized towards the end of this section. A more complete description of these wave fluxes associated with tsunamis is given by Hickey et al. (2010b).
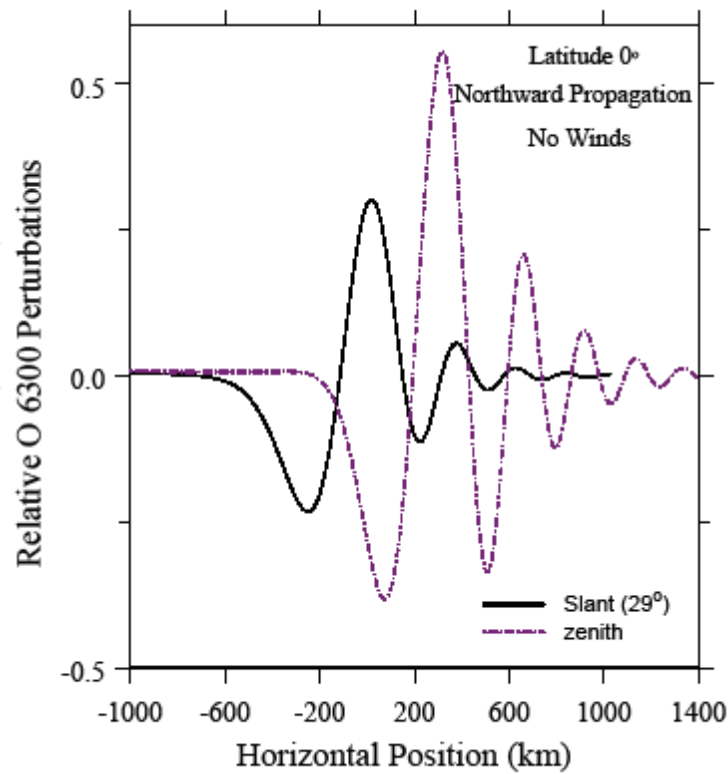
Fig. 10a. OI 6300 Å relative brightness fluctuations for overhead and oblique viewing (after Hickey et al., 2010a)
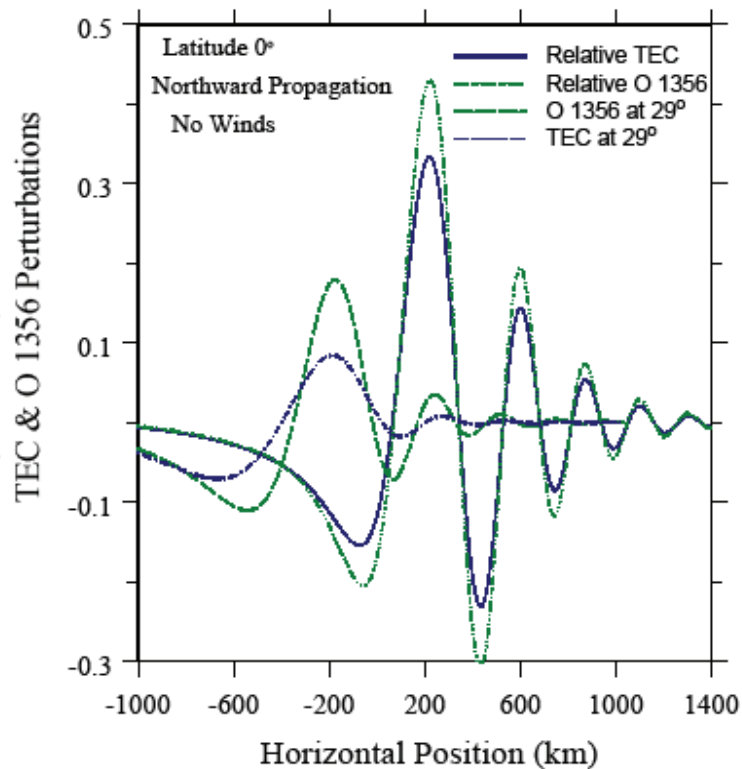

Fig. 10b. Relative total electron content and O 1356 Å fluctuations for overhead and oblique viewing (after Hickey et al., 2010a)

The non-acceleration conditions are that the waves be steady, linear, non-dissipating, and do not encounter critical levels (Walterscheid, 1995). For waves that satisfy the non-acceleration conditions the wave fluxes remain constant as the waves propagate upward. If these conditions are violated, the wave fluxes will change with height and the atmosphere can be irreversibly altered (eventually relaxing to a new steady-state). In particular, waves propagating into the thermosphere will eventually be viscously damped and a convergence of the momentum flux will occur, with a concomitant acceleration of the mean state given by

$$\frac{\partial \bar{u}_2}{\partial t} = -\frac{1}{\bar{\rho}} \frac{d}{dz} \left(\bar{\rho} \langle u'w' \rangle \right) \tag{12}$$

Here $\bar{u}_2$ is the second order, horizontally averaged change in mean state velocity associated with gravity wave forcing. This forcing is important in the terrestrial mesosphere, but in this case it is the wave amplitudes becoming nonlinear with subsequent wave breaking that leads to a momentum flux convergence. Fast gravity waves, such as those associated with tsunamis, should experience a large amplitude growth as they propagate upward through the thermosphere because they have large vertical wavelengths and so are far less dissipated than slower waves. Because they can attain large amplitudes in the middle thermosphere, their eventual dissipation might lead to large values of $\bar{u}_2$.

The major part of the gravity wave disturbance shown previously in Figure (5a) lies in a horizontal region of approximately 800 km extent. We calculate horizontal averages of wave fluxes over this horizontal extent in order to determine the second-order forcing of the atmosphere. Specifically, for a physical quantity ψ', we calculate the horizontally averaged vertical flux by evaluating

$$\langle w'\psi' \rangle = \frac{1}{N} \sum_{j=1}^{N} \mathrm{Re}(w'_j) \mathrm{Re}(\psi'_j) \tag{13}$$

In Equation (13), j is an index denoting the horizontal position of the physical variables w'_j and ψ'_j calculated from an inverse discrete Fourier transform over all waves in the spectrum. Also, N is the number of points at which the variables are evaluated over the 800 km horizontal extent of the disturbance.

The disturbance momentum flux per unit mass ($<u'w'>$) is shown in Figure 11a. At all altitudes shown it is negative and in the same direction as the phase propagation. Its magnitude increases with increasing height in the thermosphere, achieving a maximum value of ~ 1800 m^2 s^{-2} near 230 km altitude, and decreasing at greater heights due to viscous dissipation. The associated mean state acceleration is shown in Figure 11b. It maximizes in the middle thermosphere (near 250 km altitude) with a value of ~ 230 m s^{-1} h^{-1} (in the same direction as the phase velocity) and with a full-width at half maximum of ~ 120 km. Hence the dissipating disturbance drives a deep region of the thermosphere. Because the dominant part of the disturbance is of ~ 800 km horizontal extent (which is twice the dominant horizontal wavelength in the spectrum), the forcing would occur for ~ 1 h (two wave periods). Hence the acceleration shown in Figure 11b can be interpreted as the estimated change in velocity of this region of the thermosphere. This forcing would be applied over a large area (8000 km along-track for 10 h of propagation, and over a broad lateral extent). The

viscous relaxation time was estimated by Hickey et al. (2010b) to be ~ 10 h near 200 km altitude and a few tens of minutes near 300 km altitude. Hence the high altitude (> 250 km) acceleration shown in Figure 11b is probably an overestimate. Note that because the wave forcing is second order, it is proportional to the square of the wave amplitude. Hence, only the largest amplitude tsunamis may be able to produce such large mean state forcing of the thermosphere.

The sensible heat flux has been previously discussed in the literature (Walterscheid, 1981, 1995) and was calculated by Hickey et al. (2010b) for the tsunamigenic disturbance related to the Sumatra 2004 event. In this case the atmospheric heating and cooling due to the dissipating disturbance (not shown) was found to be ~ +25 K h^{-1} near 180 km altitude, and -25 K h^{-1} near 290 km altitude. The expected temperature changes are relatively small compared to the undisturbed mean state temperature (~ 753 K) and may be too small to be unambiguously identified in observations.
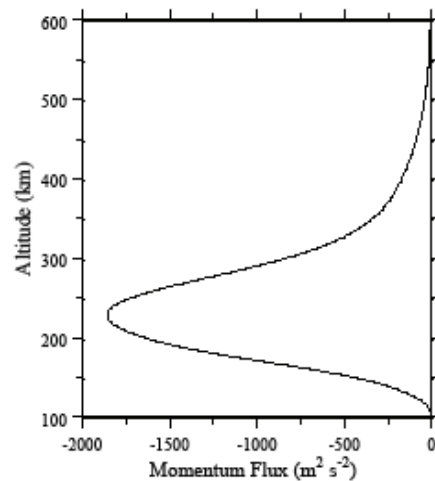

Fig. 11a. Disturbance momentum flux (m^2 s^{-2}) (after Hickey et al., 2010b)
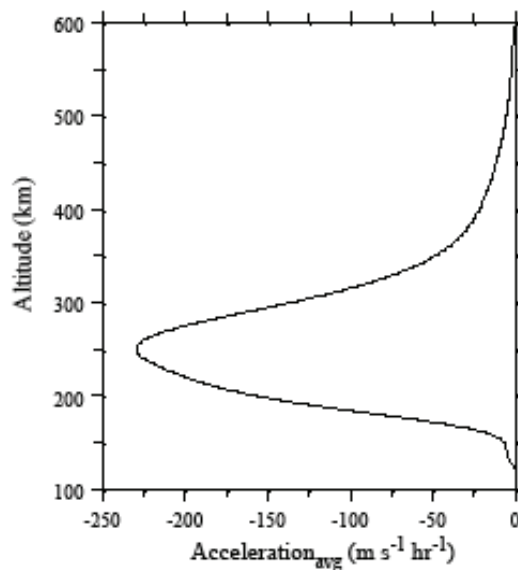

Fig. 11b. Horizontally averaged mean state acceleration due to the divergence of the disturbance momentum flux (after Hickey et al., 2010b)

6. Discussion

We have used a linear model to describe the gravity wave disturbance. For the motions of the neutral atmosphere considered here this is a reasonable assumption. Orlanski and Bryan (1969) showed that a criterion for the onset of convective instability is $u' > c$, where u' is the horizontal velocity perturbation and c is the horizontal phase speed of the wave. We find that the maximum value of u' is ~ 100 m/s, while c is 200 m/s. However, the ionospheric perturbations we have obtained are quite large, up to ~60% of the mean for realistic dissipation included, for which the assumption of linearity is violated. Nonetheless, we expect the results obtained to provide an overall good description of the expected ionospheric response. Future work should include a nonlinear treatment of this aspect of the model.

The work described herein was based on an assumed shallow water phase speed of 200 m/s and an ocean depth of ~ 4 km. Further numerical experimentation (not shown) has investigated the effect of changing this phase speed. Decreasing the phase speed results in a decrease in the vertical wavelength of the gravity waves in the spectrum. This leads to an increase in the viscous dissipation rate of the waves in the thermosphere. Because of this, these waves do not penetrate as far into the thermosphere as the faster waves do, and so achieve smaller amplitudes. Increasing the phase speed brings the waves closer to evanescence over much of the mesosphere (see discussion in Hickey et al., 2009), and so somewhat impedes their propagation to greater altitudes. Hence, we find that 200 m/s is close to an optimum phase speed for efficient gravity wave propagation from the lower atmosphere to the thermosphere. This in turn implies that the ionospheric response to tsunamis should maximize in regions where the ocean depth is ~ 4 km.

7. Conclusions

Tsunamis are a relatively rare event, but nonetheless in some instances they may have large, dramatic effects on the upper atmosphere. In addition to causing large fluctuations in electron density and in the total electron content, they will also cause comparable fluctuations in natural airglow emissions, such as the OI 6300 A and O 1356 A emissions. These airglow emissions could be observed from the ground and from space, and could help provide additional information leading to the early detection of tsunamis. The disturbances may, at times, carry significant wave momentum to F-region altitudes leading to strong accelerations of the mean flow. The observations of such events may offer an excellent opportunity of testing gravity wave theories and models, and we suggest that dedicated observations should be considered for future programs to study lower-upper atmosphere coupling and to better understand the role of tsunamis in this process.

8. Acknowledgements

9. References

Abe, K. (2006). Dominant periods of the 2004 Sumatra tsunami and the estimated source size, *Earth Planets Space*, *58*, 217-221.

Artru, J., V. Ducic, H. Kanamori, P. Lognonne, and M. Murakami (2005a). Ionospheric detection of gravity waves induced by tsunamis, *Geophys. J. Int.*, *160*, 840-848.

Artru, J., P. Lognonne, G. Occhipinti, F. Crespon, R. Garcia, E. Jeansou, and M. Murakami (2005b). Tsunami detection in the ionosphere, *Space Res. Today*, *163*, 23-27.

Bruce, G. H., D. W. Peaceman, H. H. Rachford, Jr., and J. D. Rice (1953). Calculations of unsteady-state gas flow through porous media, *Petrol. Trans. AIME, 198*, 79-92.

DasGupta, A., Das., A., Hui, D., Bandyopadhyay, K. K., and Sivaraman, M. R. (2006). Ionospheric perturbation observed by the GPS following the December 26th, 2004 Sumatra-Andaman earthquake, *Earth Planets Space*, *35*, 929-959.

DeMajistre, R., Paxton, L. J., and Bilitza, D. (2007). Comparison of ionospheric measurements made by digisondes with those inferred from ultraviolet airglow, *Adv. Space Res.*, *39*, 918-925.

Fritts, D. C., and Alexander, M. J. (2003). Gravity wave dynamics and effects in the middle atmosphere, *Rev. Geophys.*, 41(1), 1003, doi:10.1029/2001RG000106.

Georges, T. M. (1968). HF Doppler studies of traveling ionospheric disturbances, *J. Atmos. Terr. Phys.*, *30*, 735-746.

Hébert, H., Sladen, A., and Schindelé, F. (2007). Numerical modeling of the great 2004 Indian Ocean tsunami: Focus on the Mascarene Islands. *Bull. Seismol. Soc. Am.*, *97*, 1A, S208-S222.

Hedin, A. E. (1991). Extension of the MSIS thermosphere model into the middle and lower atmosphere, *J. Geophys. Res.*, *96*, 1159.

Hedin, A. E., et al. (1996). Empirical wind model for the upper, middle and lower atmosphere, *J. Atmos. Terr. Phys.*, *58*, 1421.

Hickey, M. P. and Cole, K. D. (1987). A Quartic Dispersion Equation for Internal Gravity waves in the Thermosphere. *J. Atmos. Terr. Phys., 49*, 889.

Hickey, M. P., Walterscheid, R. L. and Schubert, G. (2004). Erratum to "Gravity Wave Heating and Cooling in Jupiter's Thermosphere", *Icarus, 170*, 524-525.

Hickey, M. P., Walterscheid, R. L., Taylor, M. J., Ward, W., Schubert, G., Zhou, Q., Garcia, F., Kelley, M. C., and Shepherd, G. G. (1997). Numerical Simulations of Gravity Waves Imaged over Arecibo during the 10-day January 1993 Campaign, *J. Geophys. Res., 102*, 11,475.

Hickey, M. P., Schubert, G., and Walterscheid, R. L. (2009). The Propagation of Tsunami-Driven Gravity Waves into the Thermosphere and Ionosphere, *J. Geophys. Res., 114*, A08304, doi:10.1029/2009JA014105.

Hickey, M. P., Schubert, G., and Walterscheid, R. L. (2010a). Atmospheric airglow fluctuations due to a tsunami-driven gravity wave disturbance, *J. Geophys. Res., 115*, A06308, doi:10.1029/2009JA014977.

Hickey, M. P., Walterscheid, R. L. and Schubert, G. (2010b). Wave mean flow interactions in the thermosphere induced by a major tsunami, *J. Geophys. Res., 115*, A09309, doi:10.1029/2009JA014927.

Hines, C. O. (1960). Internal atmospheric gravity waves at ionospheric heights, *Can. J. Phys.*, 38, 1441.

Hines, C. O. (1972). Gravity waves in the atmosphere, *Nature, 239*, 73-78.

Hines, C. O. (1968). An effect of molecular dissipation in upper atmospheric gravity waves, *J. Atmos. Terr. Phys.*, *30*, 845-849.

Hooke, W. H. (1968). Ionospheric irregularities produced by internal atmospheric gravity waves. *J. Atmos. Sol. Terr. Phys.*, *30*, 795-823.

Kelley, M. C. (1989). *The Earth's Ionosphere*, Academic Press Inc.

Kubota, M., Kukunishi, H., and Okano, S. (2001). Characteristics of medium- and large-scale TIDs over Japan derived from OI 630-nm nightglow observations, *Earth Planets Space*, *53*, 741-751.

Lee, M. C., Pradipta, R., Burke, W. J., Labno, A., Burton, L. M., Cohen, J. A., Dorfman, S. E., Coster, A. J., Sulzer, M. P., and Kuo, S. P. (2008). Did tsunami-launched gravity waves trigger ionospheric turbulence over Arecibo? *J. Geophys. Res.*, *113*, A01302, doi:10.1029/2007JA012615.

Lighthill, J. (1978). *Waves in Fluids*, Cambridge University Press, Cambridge.

Lindzen, R. S., and H. L. Kuo (1969). A reliable method for the numerical integration of a large class of ordinary and partial differential equations. *Mon. Wea. Rev.*, 97, 732-734.

Liu, J., Tsai, Y., Chen, S., Lee, C., Chen, Y., Yen, H., Chang, W., and Liu, C. (2006a). Giant ionospheric disturbances excited by the M9.3 Sumatra earthquake of 26 December 2004. *Geophys. Res. Lett.*, *33*, L021103, doi:10.1029/2005GL023963.

Liu, J., Tsai, Y., Ma, K., Chen, Y., Tsai, H., Lin, C., Kamogawa, M., and Lee, C. (2006b). Ionospheric GPS total electron content (TEC) disturbances triggered by the 26 December 2004 Indian Ocean tsunami, *J. Geophys. Res.*, *111*, A05303, doi:10.1029/2005JA011200.

Martyn, D. F. (1950). Cellular atmospheric waves in the ionosphere and troposphere, *Proc. Roy. Soc.*, A201, 216.

McLeod, M. A. (1965). Sporadic E Theory. I. Collision-Geomagnetic Equilibrium, *J. Atmos. Sci.*, *23*, 96-109.

Mendillo, M., Baumgardner, J., Nottingham, D., Aarons, J., Reinisch, B., Scali, J., and Kelley, M. C. (1997). Investigations of thermospheric-ionospheric dynamics with 6300-Å images from the Arecibo Observatory, *J. Geophys. Res.*, *102*, 7331-7343.

Munro, G. H. (1948). Short period changes in the F-region of the ionosphere, *Nature*, 162, 886.

Occhipinti, G., P. Lognonne, E. A. Kherani, and H. Hebert (2006). Three-dimensional waveform modeling of ionospheric signature induced by the 2004 Sumatra tsunami, *Geophys. Res. Lett., 33*, L20104, doi::10.1029/2006GL026865.

Occhipinti, G., E., A. Kherani , and P. Lognonne (2008). Geomagnetic dependence of ionospheric disturbances induced by tsunamigenic internal gravity waves, *Geophys. J. Int.*, 173, 753-765.

Orlanski, I., and Bryan, K. (1969). Formation of the thermocline step structure by large-amplitude internal gravity waves, *J. Geophys. Res.*, *74*, 6975-6983.

Parish, H. F., Schubert, G., Hickey, M. P., and Walterscheid, R. L. (2009). Propagation of tropospheric gravity waves into the upper atmosphere of Mars, *Icarus*, doi:10.1016/j.icarus.2009.04.031.

Paxton, L. J., Morrison, D., Strickland, D. J., McHarg, M. J., Zhang, Y., Wolven, B., Kil, H., Crowley, G., Christensen, A. B., and Meng, C.-I. (2003). The use of far ultraviolet remote sensing to monitor space weather, *Adv. Space Res.*, *31*(4), 813-818.

Peltier, W. R., and Hines, C. O. (1976). On the possible detection of tsunamis by a monitoring of the ionosphere, *J. Geophys. Res.*, *81*, 1995-2000.

Schubert, G., Hickey, M. P., and Walterscheid, R. L. (2003). Heating of Jupiter's thermosphere by the dissipation of upward propagating acoustic waves, *Icarus., 163*, 398-413.

Schubert, G., M. P. Hickey, and R. L. Walterscheid (2005). Physical processes in acoustic wave heating of the thermosphere, *J. Geophys. Res.*, *110*, D07106, doi:10.1029/2004JD005488.

Schunk, R. and J. Sojka (1996). USU model of the global ionosphere, in *STEP: Handb. of Ionospheric Models*, Ed. R.W. Schunk, SCOSTEP.

Scorer, R. S. (1949). Theory of waves in the lee of mountains, *Q. J. Roy. Met. Soc.*, *75*, 323, 41-56.

Walterscheid, R. L., G. Schubert, and J. Straus (1987). A dynamical-chemical model of wave-driven fluctuations in the OH nightglow, *J. Geophys. Res.*, *92*, 1241-1254.

Walterscheid, R. L., and M. P. Hickey (2001). One-gas models with height-dependent mean molecular weight: Effects on gravity wave propagation, *J. Geophys. Res.*, *106*, 28,831-28,839.

Wilson, M. (2005). Modeling the Sumatra-Andaman earthquake reveals a complex, nonuniform rupture, *Phys. Today*, *58*, 19.

10. Appendix 1.

	Ion Reaction	Rate (cm^3 s^{-1})
1	$O^+ + N_2 \rightarrow NO^+ + N$	$k_1 = 5 \times 10^{-13}$
2	$O^+ + O_2 \rightarrow O_2^+ + O$	$k_2 = 2 \times 10^{-11} (T/300)^{-0.4}$
3	$O^+ + NO \rightarrow NO^+ + O$	$k_3 = 8 \times 10^{-13}$
4	$O^+ + e \rightarrow O(^5P) + \hbar\nu_{1356}$	$k_4 = 7.3 \times 10^{-13}$
5	$O_2^+ + N_2 \rightarrow NO^+ + NO$	$k_5 = 5 \times 10^{-16}$
6	$O_2^+ + NO \rightarrow NO^+ + O_2$	$k_6 = 4.4 \times 10^{-10}$
7a	$O_2^+ + e \rightarrow O + O(^3P)$	$k_{7a} = 0.62 \times 1.6 \times 10^{-7} (300/T)^{0.55}$
7b	$O_2^+ + e \rightarrow O + O(^1S)$	$k_{7b} = 0.08 \times 1.6 \times 10^{-7} (300/T)^{0.55}$
7c	$O_2^+ + e \rightarrow O + O(^1D)$	$k_{7c} = 1.30 \times 1.6 \times 10^{-7} (300/T)^{0.55}$
8	$N_2^+ + O \rightarrow NO^+ + N$	$k_8 = 1.4 \times 10^{-10} (300/T)^{0.44}$
9	$N_2^+ + O \rightarrow O^+ + N_2$	$k_9 = 1 \times 10^{-11} (300/T)^{0.23}$
10	$N_2^+ + O_2 \rightarrow O_2^+ + N_2$	$k_{10} = 5 \times 10^{-11} (300/T)^{-1}$
11	$N_2^+ + NO \rightarrow NO^+ + N_2$	$k_{11} = 3.3 \times 10^{-10}$
12	$N_2^+ + e \rightarrow N + N$	$k_{12} = 1.8 \times 10^{-7} (300/T)^{0.39}$
13	$NO^+ + e \rightarrow N + O$	$k_{13} = 4.2 \times 10^{-7} (300/T)^{0.85}$
14	$O(^1S) \rightarrow O(^1D) + \hbar\nu_{5577}$	$A_{5577} = 1.06$ s^{-1}
15a	$O(^1D) \rightarrow O(^3P) + \hbar\nu$	$A_{6300+6364} = 9.34 \times 10^{-3}$ s^{-1}
15b	$O(^1D) \rightarrow O(^3P) + \hbar\nu_{6300}$	$A_{6300} = 7.1 \times 10^{-3}$ s^{-1}
16	$O(^1D) + N_2 \rightarrow O + N_2$	$k_{16} = 2.0 \times 10^{-11} \exp[107.8/T]$
17	$O(^1D) + O_2 \rightarrow O + O_2$	$k_{17} = 2.0 \times 10^{-11} \exp[67.5/T]$
18	$O(^1D) + O \rightarrow O + O$	$k_{18} = 8.0 \times 10^{-12}$

Table 1. Chemical reactions for ions (after Hickey et al., 2010a)

The Tsunami Threat - Research and Technology

Edited by Nils-Axel Mörner

Submarine earthquakes, submarine slides and impacts may set large water volumes in motion characterized by very long wavelengths and a very high speed of lateral displacement, when reaching shallower water the wave breaks in over land - often with disastrous effects. This natural phenomenon is known as a tsunami event. By December 26, 2004, an event in the Indian Ocean, this word suddenly became known to the public. The effects were indeed disastrous and 227,898 people were killed. Tsunami events are a natural part of the Earth's geophysical system. There have been numerous events in the past and they will continue to be a threat to humanity; even more so today, when the coastal zone is occupied by so much more human activity and many more people. Therefore, tsunamis pose a very serious threat to humanity. The only way for us to face this threat is by increased knowledge so that we can meet future events by efficient warning systems and aid organizations. This book offers extensive and new information on tsunamis; their origin, history, effects, monitoring, hazards assessment and proposed handling with respect to precaution. Only through knowledge do we know how to behave in a wise manner. This book should be a well of tsunami knowledge for a long time, we hope.

How to reference

In order to correctly reference this scholarly work, feel free to copy and paste the following:

Michael P. Hickey (2011). Atmospheric Gravity Waves and Effects in the Upper Atmosphere Associated with Tsunamis, The Tsunami Threat - Research and Technology, Nils-Axel Mörner (Ed.), ISBN: 978-953-307-552-5, InTech, Available from: http://www.intechopen.com/books/the-tsunami-threat-research-and-technology/atmospheric-gravity-waves-and-effects-in-the-upper-atmosphere-associated-with-tsunamis

INTECH
open science | open minds